LITHOS 454-455 (2023) 107281

Contents lists available at ScienceDirect

LITHOS

journal homepage: www.elsevier.com/locate/lithos

Transcrustal magma plumbing process in the Cenozoic Dali potassic lamprophyre dyke formation in the southeastern Tibet Plateau

Shitao Zhang [a,b], Xiaoping Long [a,*], Fangyi Zhang [c], Le Zhang [d]

[a] State Key Laboratory of Continental Dynamics, Department of Geology, Northwest University, Xi'an 710069, China
[b] State Key Laboratory of Ore Deposit Geochemistry, Institute of Geochemistry, Chinese Academy of Sciences, Guiyang 550081, China
[c] Center of Deep-Sea Research, Institute of Oceanology, Chinese Academy of Sciences, Qingdao 266071, China
[d] State Key Laboratory of Isotope Geochemistry, Guangzhou Institute of Geochemistry, Chinese Academy of Sciences, Guangzhou 510640, China

ARTICLE INFO

Keywords:
Lamprophyre
Clinopyroxene
Oscillatory zoning
Transcrustal magmatic processes

ABSTRACT

(Ultra-)potassic lamprophyres are volumetrically rare, but are widely distributed in diverse geological settings and extensively applied to trace the mantle source and melting processes. However, it is still debatable whether the lamprophyre formation involved transcrustal magmatic processes. In this study, we describe the diverse zoning patterns and textures of clinopyroxene (Cpx) from a Cenozoic potassic lamprophyre dyke in southeastern Tibet Plateau. Three types of Cpx macrocrysts with normal- and reverse oscillatory zoning and sieved textures, and Cpx microcrysts from Cpx–Phl nodules are recognized. The Cpx macrocrysts have highly variable Mg# (62–89) and chemical compositions. Their oscillatory-zoned mantle has alternating coarse layers or closely-packed layers, with distinct resorption surface shown in backscattered electron (BSE) images. High-amplitude oscillation of Mg# (±5 to ±12), Al, Cr and Sr at the boundary layers of mantle may reflect multiple magma mixing/recharge events. In contrast, low-amplitude and high-frequency oscillation of Mg# (varying from < ±3) across the closely-packed layers could be attributed to local magma mixing or kinetic effect at the crystal-melt interface. The sieved domains occur in the Cpx macrocrystic core with spongy space and linking the external groundmass by cracks, and have major and minor compositions and $^{87}Sr/^{86}Sr$ ratios similar to those of the rims. This indicates that the sieved domains are probably originated from dissolution of the Cpx macrocrysts by groundmass melt and later reprecipitation. The estimated pressure and temperature for the Cpx macrocryst high-Mg# cores and low Mg# rims are 580–1160 MPa (avg. 919 MPa) and 30–1270 MPa (avg. 681 MPa), and 1116–1266 °C (avg. 1216 °C) and 955–1215 °C (avg. 1110 °C), respectively, suggesting polybaric differentiation or Cpx-saturated magmas. The estimated pressure and temperature for the reverse-zoned Cpx marcocryst cores are 450–1310 MPa (avg. 953 MPa) and 1097–1209 °C (avg. 1166 °C), respectively, indicating that they are likely formed in equilibrium with a more evolved magma batch, and then were entrapped by more primitive mantle-derived potassic magmas during magma upwelling. The La/Yb and Dy/Yb modelling of equilibrium melts suggest that magmas of the Cpx–Phl nodules and their lamprophyre host were derived from similar mantle sources. Therefore, the complex zoning patterns and compositions of Cpx macrocrysts could indicate transcrustal magmatic processes in the potassic lamprophyre dyke formation.

1. Introduction

Lamprophyre is a special group of hypabyssal porphyritic dykes with mafic phenocrysts (e.g., mica, pyroxene and/or amphibole) and is typified by the absence of felsic phenocrysts (Le Maitre et al., 2002; Rock, 1977). Lamprophyres are volumetrically rare, but were reported in various geological settings, such as orogenic belts and within-plate settings (Imaoka et al., 2017; Karsli et al., 2014; Rock, 1991). They usually contain magmatic enclaves, cumulate nodules, crustal and mantle-derived xenoliths and xenocrysts, providing clues for their petrogenesis and deep crustal geodynamic processes (Li et al., 2021; Liu et al., 2013; Semiz et al., 2012; Soltanmohammadi et al., 2021; Zhang et al., 2021). Published geochemical data show that lamprophyres are commonly more enriched in volatiles, alkalis and other incompatible

* Corresponding author at: State Key Laboratory of Continental Dynamics, Department of Geology, Northwest University, Northern Taibai Str. 229, Xi'an 710069, China.
E-mail address: longxp@nwu.edu.cn (X. Long).

https://doi.org/10.1016/j.lithos.2023.107281
Received 24 December 2022; Received in revised form 8 July 2023; Accepted 8 July 2023
Available online 13 July 2023

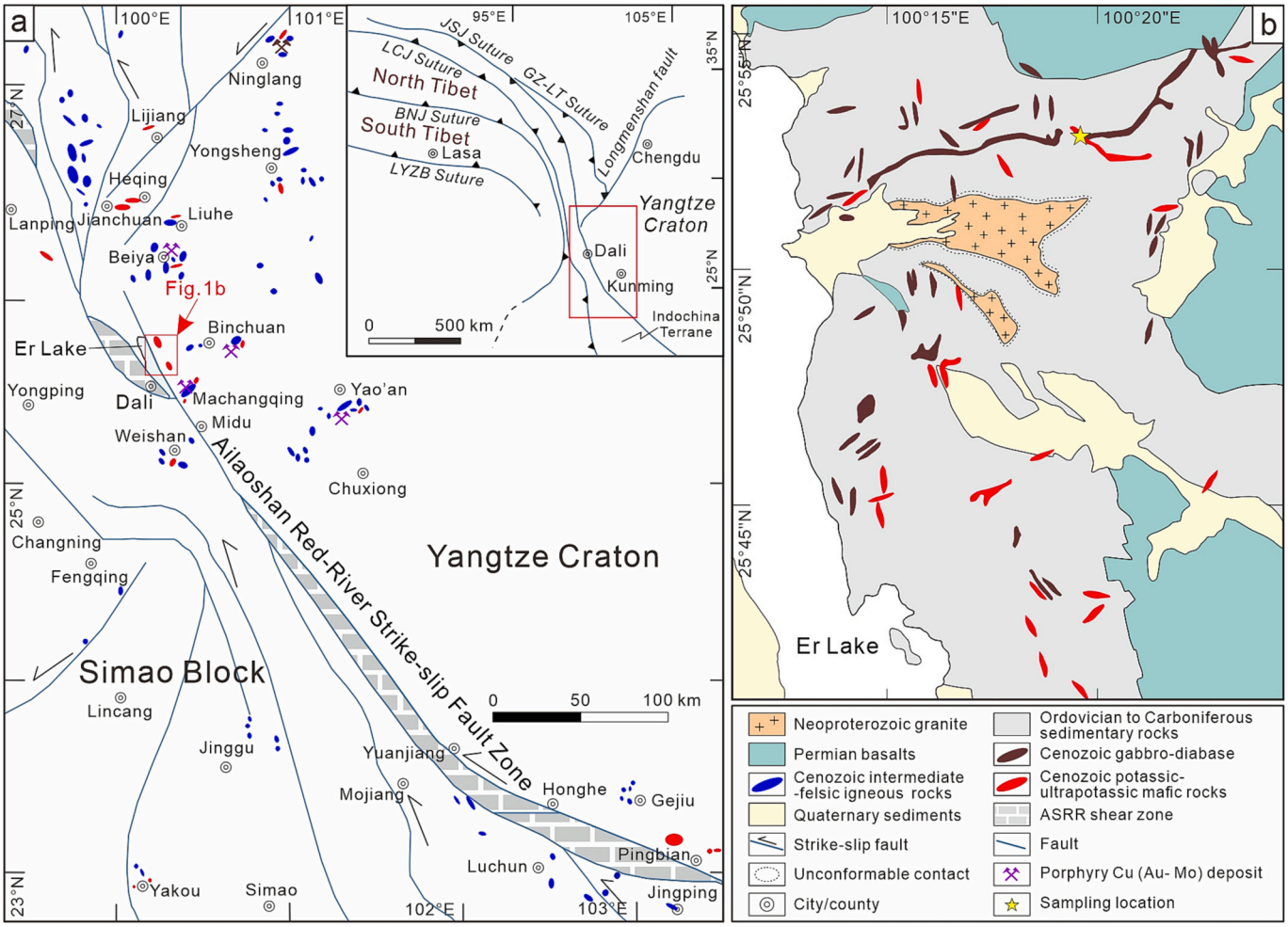

Fig. 1. (a) Simplified tectonic framework of the southeastern margin of Tibet Plateau, with the inset showing the regional tectonic context; (b) Geological map of eastern Dali in Yunnan Province, China, showing the distribution of Cenozoic igneous rocks and lamprophyre sample locations (modified after Huang et al., 2010). Suture zones: JSJ = Jinshajiang; GZ–LT = Ganzi–Litang; LCJ = Lancangjiang; BNJ = Bangong Nujiang; YLZB = Yarlung Zangbo.

elements (e.g., F, Cl, Rb, Ba, Sr and LREEs) than other silicate igneous rocks, and are potassic to ultrapotassic (e.g., Foley et al., 1987; Ma et al., 2014; Tappe et al., 2006). Consequently, their petrographic and geochemical characteristics can constrain the magma source (mantle nature, degree of partial melting and metasomatism), fractionation and crustal assimilation, as well as the dynamics and mixing processes (Casetta et al., 2019; Foley, 1992a, 1992b; Huang et al., 2010; Humphreys et al., 2006; Lu et al., 2015; Muravyeva et al., 2014; Prelevic et al., 2005; Xing and Wang, 2020; Yang and Jiang, 2018).

Previous studies have revealed that much of the shallow portions of plumbing systems beneath common basaltic to rhyolitic volcanoes is likely occupied by crystal-rich or crystal mush zone (Miller and Wark, 2007). The crystal mush zone may have maintained its semi-solidified state by heating from the underlying intermediate-mafic melt, which constitute a transcrustal magmatic plumbing system (Cashman et al., 2017; Miller and Wark, 2007). Phenocrysts of plagioclase, hornblende and/or clinopyroxene in volcanic rocks with textural and compositional zoning can record the open-system magmatic processes, including crystallization, magma recharge/mixing, decompression and convection prior to the eruption (Ginibre et al., 2002a, 2007; Humphreys et al., 2006; Ubide et al., 2014; Ubide and Kamber, 2018; Xing and Wang, 2020). Nevertheless, transcrustal magmatic processes recorded by (ultra-)potassic lamprophyres are rarely reported (Prelevic et al., 2012; Xing and Wang, 2020).

In this study, we investigate the diverse zoning patterns and textures of Cpx macrocrysts and microcrysts from the Cpx–Phl nodules and their lamprophyre dyke host at Dali in the southeastern Tibet Plateau, SW China. Integrating in situ apatite U—Pb dating, and whole-rock geochemical and Sr–Nd–Pb isotope analyses, we present the compositional variations, Mg# profile and in situ Sr isotope compositions of Cpx macrocrysts from this lamprophyre dyke. With these new data, we propose a magma mixing model for the formation of these Cenozoic potassic lamprophyre dykes in the southeastern Tibet Plateau.

2. Geological background

Dali is located in the southeastern margin of Tibetan Plateau (Fig. 1a; Huang et al., 2010; Lu et al., 2015). Due to the early Cenozoic (ca. 65–60 Ma) India-Asia collision, the regional compression is accommodated by crustal shortening and thickening, and the development of SE-trending fault systems, notably the Ailaoshan–Red River fault zone (Fig. 1a; Chung et al., 2005; Wang et al., 2021). The fault zone is a large sinistral strike-slip shear (500–700 km long), representing the South China-Indochina suture and linking with the Jinshajiang suture zone to the north (Fig. 1a; Chung et al., 2005; Lu et al., 2015; Xu et al., 2021).

(Ultra-)potassic magmatic rocks, including lamprophyres, trachybasalt- trachyandesite, shoshonite, leucite, latite, trachyte and potassic granitoids, are widely exposed in the southeastern Tibet Plateau, especially in the northern end of the Ailaoshan–Red River fault zone (Fig. 1a; Guo et al., 2005; Huang et al., 2010; Lu et al., 2015; Shen et al., 2021; Wang et al., 2021). The (ultra-)potassic mafic rocks occur primarily as fault-controlled volcanic dykes or pipes (Fig. 1a). The potassic granitoids

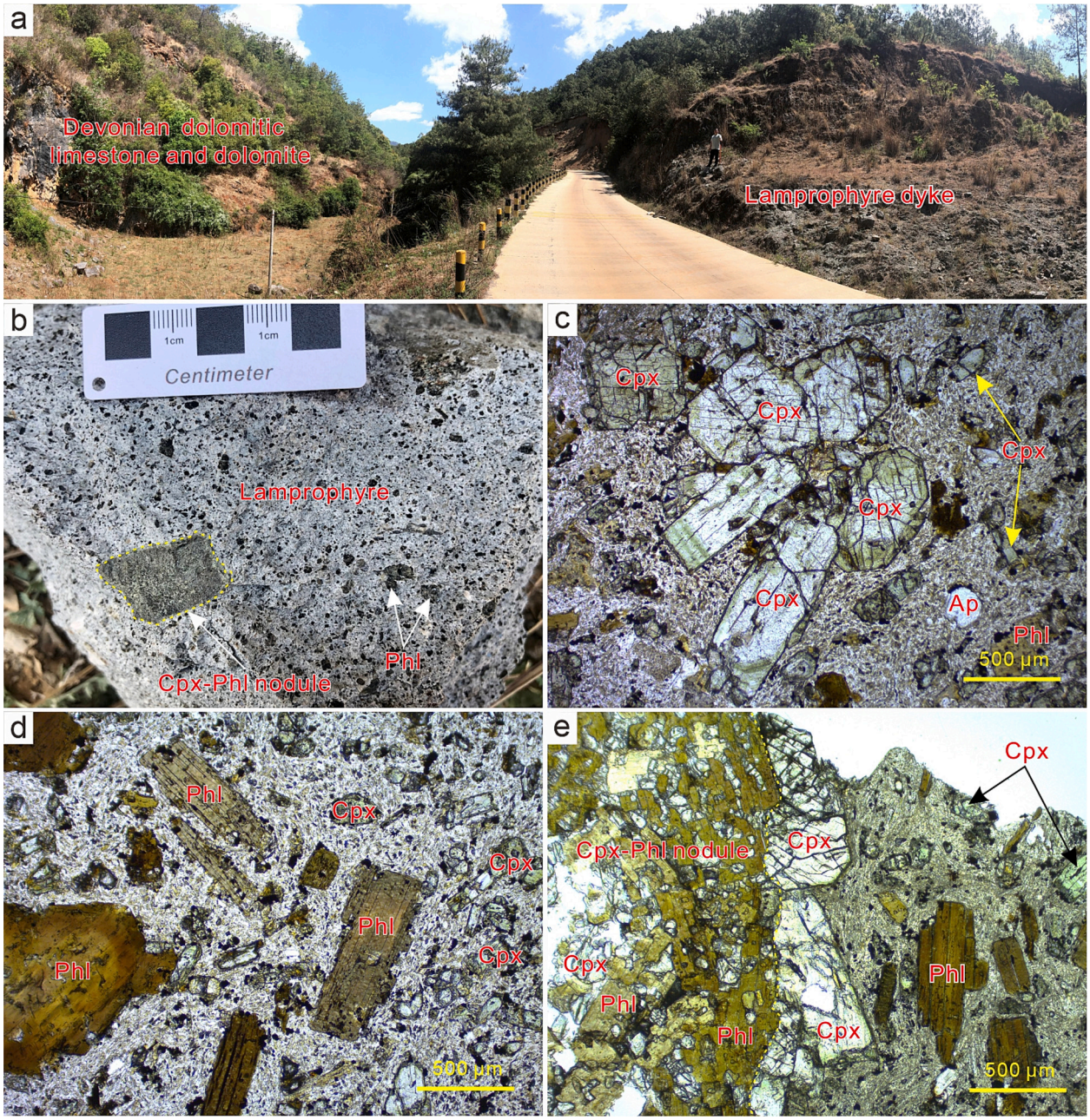

Fig. 2. Photographs and photomicrographs showing field outcrops and petrographic features of the Cpx–Phl nodules and their lamprophyre host at Dali: (a) Outcrops of lamprophyre dyke intruding the Devonian dolomite-dolomitic limestone; (b) Ellipsoidal Cpx–Phl nodules in lamprophyre dyke; (c) Cpx macrocrysts with oscillatory zoning texture in lamprophyre dyke; (d) Phl macrocrysts with oscillatory zoning texture in lamprophyre dyke; (e) Contact between Cpx–Phl nodule and lamprophyre host. Abbreviations: Cpx = clinopyroxene; Phl = phlogopite.

include (mainly porphyritic) syenite, monzonite and granite, associated with skarn−/porphyry-type Au–Cu–Mo mineralization, such as the Beiya, Yao'an and Machangqing ore deposits (Wang et al., 2021; Xu et al., 2021). Many of these (ultra-)potassic magmatic units were dated at 40–30 Ma by using zircon/titanite U—Pb and phlogopite Ar—Ar geochronology (Huang et al., 2010; Lu et al., 2015; Wang et al., 2021; Xu et al., 2021).

The study area lies in the eastern Erhai district at Dali, SW Yunnan Province, China (Fig. 1a, b). The exposed strata are mainly Ordovician quartz sandstone to arenaceous shale, and Devonian-Lower Permian carbonate and siliceous rocks, whereas Mesozoic strata are absent (Fig. 1b; Huang et al., 2010). The Neoproterozoic granite in central Dali is in nonconformity contact with the Devonian dolomite and dolomitic limestone. Late Permian Emeishan large igneous province (LIP)-related flood basalts are mainly distributed in eastern Dali (Huang et al., 2010; Lu et al., 2015). Cenozoic alkaline mafic rocks (incl. Gabbro–diabase, potassic- and ultrapotassic mafic rocks) are widely distributed in the study area (Fig. 1b).

In this study, thirteen lamprophyre samples were collected from northeastern Dali, Yunnan Province, China (Fig. 1b). The NW- to EW-trending lamprophyre dyke intruded the Devonian dolomitic limestone and dolomite, and is over 10 m wide and several km long (Figs. 1b and 2a). The samples are light grey to greyish-green and porphyritic (Fig. 2b). The lamprophyre contains ~40 vol% macrocrysts of clinopyroxene (ca. 25–30 vol%) and phlogopite (ca. 10–15 vol%) and ~ 60 vol% groundmass of K-feldspar, clinopyroxene, phlogopite, apatite and magnetite, and minor (<5 vol%) ilmenite, carbonate ocelli and vesicles (Fig. 2b-e). Therefore, the rocks can be classified as minette based on the

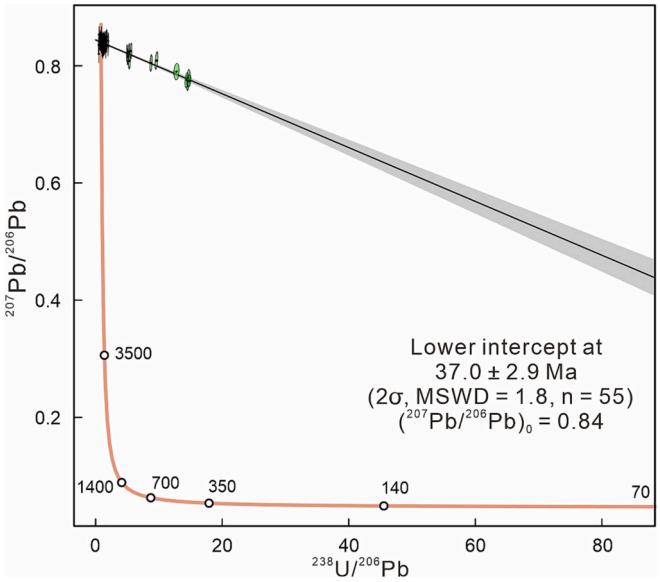

Fig. 3. LA–ICP–MS apatite U—Pb Tera-Wasserburg concordia diagram for the Dali lamprophyre.

lamprophyre classification (Le Maitre et al., 2002; Rock, 1991). Some Cpx–Phl nodules have also been identified in the lamprophyre dykes (Fig. 2b). These microgranular nodules (diameter: 2–3 cm) are dark green to black, and contain microcrysts of clinopyroxene and phlogopite with minor apatite, magnetite and vesicles (Fig. 2b, e).

3. Analytical methods

3.1. Apatite U—Pb dating

Apatite U—Pb isotope dating was determined at the Guangzhou Tuoyan Analytical Technology Co. Ltd., Guangzhou, China, by using a NWR 193 nm ArF Excimer laser-ablation system coupled to an iCAP RQ ICPMS. The ICPMS was tuned using NIST 610 standard glass to yield low oxide production rates. During the analysis, 0.7 l/min He carrier gas was fed into the cup, and the aerosol was subsequently mixed with 0.84 l/min Ar make-up gas. The laser fluence was 5 J/cm^2, with repetition rate of 6 Hz, 50 μm spot size and analysis time of 40 s, followed by a 40 s background measurement. Detailed descriptions of the geochemical methods and apatite standards are presented in Appendix A.

3.2. Whole-rocks major and trace element analyses

In this study, whole–rock major and trace element compositions and Sr–Nd–Pb isotope data for the Dali lamprophyre rock samples (avoiding Cpx–Phl nodule contamination) are listed in Appendix B. The Cpx–Phl nodules are too small to be analyzed. The analyses were carried out at the Nanjing FocuMS Technology Co. Ltd., Nanjing, China. The instruments of Agilent Technologies 5110 ICP-OES (Penang, Malaysia) and Agilent Technologies 7700× quadrupole ICP-MS (Tokyo, Japan) were used to determine the major- and minor-, and trace elements, respectively. The instrument of Nu Instruments Nu Plasma II MC-ICP-MS (Wrexham, Wales, UK) through Teledyne Cetac Technologies Aridus II desolvating nebulizer system (Nebraska, USA) was used to determine the radioactive Sr–Nd–Pb isotopes. Detailed descriptions of the geochemical methods are presented in Appendix A.

3.3. Clinopyroxene chemistry and Sr isotope analyses

The electron probe microanalysis (EPMA) of Cpx was conducted at the Key Laboratory for the Study of Focused Magmatism and Giant Ore Deposits, Xi'an Center of Geological Survey, China Geological Survey, by using a JEOL JXA-8230 EPMA. The LA–ICP–MS clinopyroxene trace element analysis was conducted at the Nanjing FocuMS Technology Co. Ltd., on an Agilent 7900a ICP–MS instrument coupled to a Resonetic 193 nm ArF excimer laser ablation system. Single spot ablation mode was adopted with 50 μm laser beam size, 120 mJ laser energy and 6 Hz ablation frequency. Then, the in situ clinopyroxene Sr isotope compositions analysis was performed on a Thermo Scientific Neptune Plus MC–ICP–MS system, coupled with a Resonetics RESOlution M-50193 nm laser ablation system at the State Key Laboratory of Isotope Geochemistry, Guangzhou Institute of Geochemistry, Chinese Academy of Sciences. The laser parameters include 82–112 μm beam diameter, 8 Hz repetition rate, and ~ 4 J/cm^2 energy density. Detailed descriptions of the geochemical methods are presented in Appendix A.

4. Results

4.1. Apatite U—Pb geochronology

Apatite U—Pb isotope data are listed in Appendix B. Table S1 and illustrated in Fig. 3. Sample 21DL03 has considerable U content (1.42–49.2 ppm, avg. 11.7 ppm). A total of 55 analytical spots yielded a Tera–Wasserburg diagram with lower intercept $^{206}Pb/^{238}U$ age of 37.0 ± 2.9 Ma (2σ, MSWD = 1.8) (Fig. 3). This age is well consistent with the whole-rock/phlogopite Ar—Ar and zircon U—Pb isotope ages for many reported Paleogene (ultra-)potassic mafic rocks (ca. 37–33 Ma) in the southeastern Tibet Plateau (e.g., Huang et al., 2010; Lu et al., 2015; Shen et al., 2021). Therefore, we suggest that this apatite U—Pb age can represent the timing of the Dali lamprophyre dyke emplacement, although apatite in the Cpx–Phl nodules are rare and too small to be U—Pb dated.

4.2. Whole-rock geochemistry

4.2.1. Major and trace element compositions

Overall, the samples have low loss on ignition (LOI = 0.96–1.63 wt %), high SiO_2 (54.81–56.21 wt%) and total alkali (K_2O + Na_2O = 8.76–9.56 wt%) contents. In the total alkali-silica classification diagram, all the samples fall into the trachyandesite field (Fig. 4a). The samples are K_2O-rich (K_2O/Na_2O = 1.70–1.77), and fall mainly into the shoshonitic series (Fig. 4b). The samples have high Al_2O_3 (13.83–14.59 wt%), CaO (4.77–6.03 wt%), FeO^T (6.38–6.87 wt%) and MgO (4.96–5.68 wt%) contents, with Mg number (Mg#) ranging from 63 to 67. In addition, they have low TiO_2 (0.78–0.85 wt%), P_2O_5 (0.36–0.61 wt%) and MnO (0.09–0.15 wt%) contents (Appendix B. Table S2).

In the chondrite-normalized rare earth element (REE) diagram, all the samples are enriched in light rare earth elements (LREEs) compared with heavy rare earth elements (HREEs), with $(La/Yb)_N$ ratios ranging from 9.80 to 12.9 (Fig. 5a). The samples have Eu/Eu* almost equal to 1 with an indistinct Eu negative anomaly (Fig. 5a). This is consistent with the absence of plagioclase fractionation. In the primitive mantle-normalized multi-element spider diagram, all the samples are characterized by enrichment of large ion lithophile elements (LILEs, e.g., Rb, Ba, K, Pb and Sr), but depletion in high field strength elements (HFSEs) (Fig. 5b).

4.2.2. Sr–Nd–Pb isotope compositions

The initial Rb—Sr, Sm—Nd and Pb isotope compositions of the Dali lamprophyre dyke were calculated based on the apatite U—Pb age (ca. 37.0 Ma) in this study. The results show that the samples are enriched in Sr—Nd isotopes, with uniform initial $^{87}Sr/^{86}Sr$ (I_{Sr}) = 0.70579 to 0.70589, $\varepsilon_{Nd}(t)$ = −2.2 to −0.9, and T_{2DM} = 925 to 1034 Ma (Appendix B. Table S3). In the I_{Sr} vs. $\varepsilon_{Nd}(t)$ diagram, the samples fall into the field of many reported (ultra-)potassic mafic units in western Yunnan (Appendix C. Fig. S1a). All the samples have low unradiogenic Pb isotope, with the calculated initial $^{206}Pb/^{204}Pb$, $^{207}Pb/^{204}Pb$ and $^{208}Pb/^{204}Pb$ ratios of

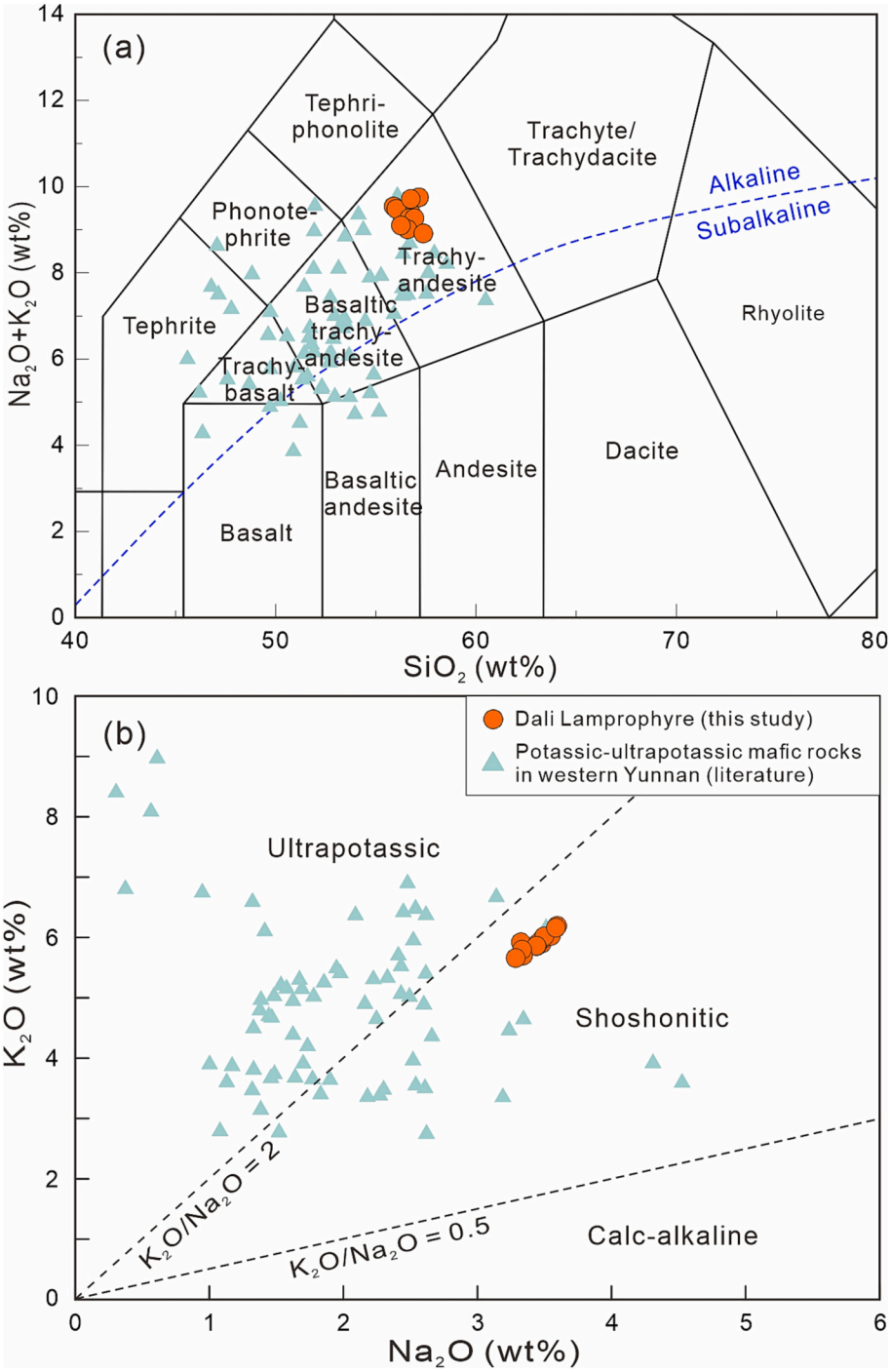

Fig. 4. (a) SiO_2 vs. (K_2O + Na_2O) (after Middlemost, 1994) and (b) Na_2O vs. K_2O plots for the Dali lamprophyre. Data for the (ultra-)potassic mafic rocks in the southeastern Tibet Plateau are from Lu et al. (2015); Yu et al. (2020) and Shen et al. (2021).

18.557–18.577, 15.615–15.621, and 38.636–38.665, respectively (Appendix C. Fig. S1b, c). They mainly fall in the western Yunnan (ultra-) potassic mafic rocks field, close to the EM2 endmember (Appendix C. Fig. S1b, c).

4.3. Clinopyroxene chemistry

4.3.1. Classification and petrographic characteristics

With BSE imaging, three types of Cpx macrocrysts (>500 μm; Zellmer, 2021) were distinguished in the Dali lamprophyre, i.e., (i) Cpx macrocryst with normal oscillatory zoning, showing a dark core, coarse/fine oscillatory zoning mantle and light-color rim (Fig. 6a-e), (ii) Cpx macrocryst with reverse oscillatory zoning, displaying a relatively light-color core, oscillatory-zoned mantle and light-color rim (Fig. 6f), and (iii) Cpx macrocryst with sieved-texture core, oscillatory-zoned mantle and light-color rim (Fig. 6g, h). The fine-grained Cpx microcrysts (<100 μm; Zellmer, 2021) are subhedral to anhedral, coexisting with phlogopite in the Cpx–Phl nodule and their lamprophyre host (Figs. 2e and 6).

4.3.2. Overall compositional variations for the different types of Cpx

A total of 420 EPMA data for clinopyroxene were obtained from ten samples of thin-sections, with detailed results shown in Appendix B.

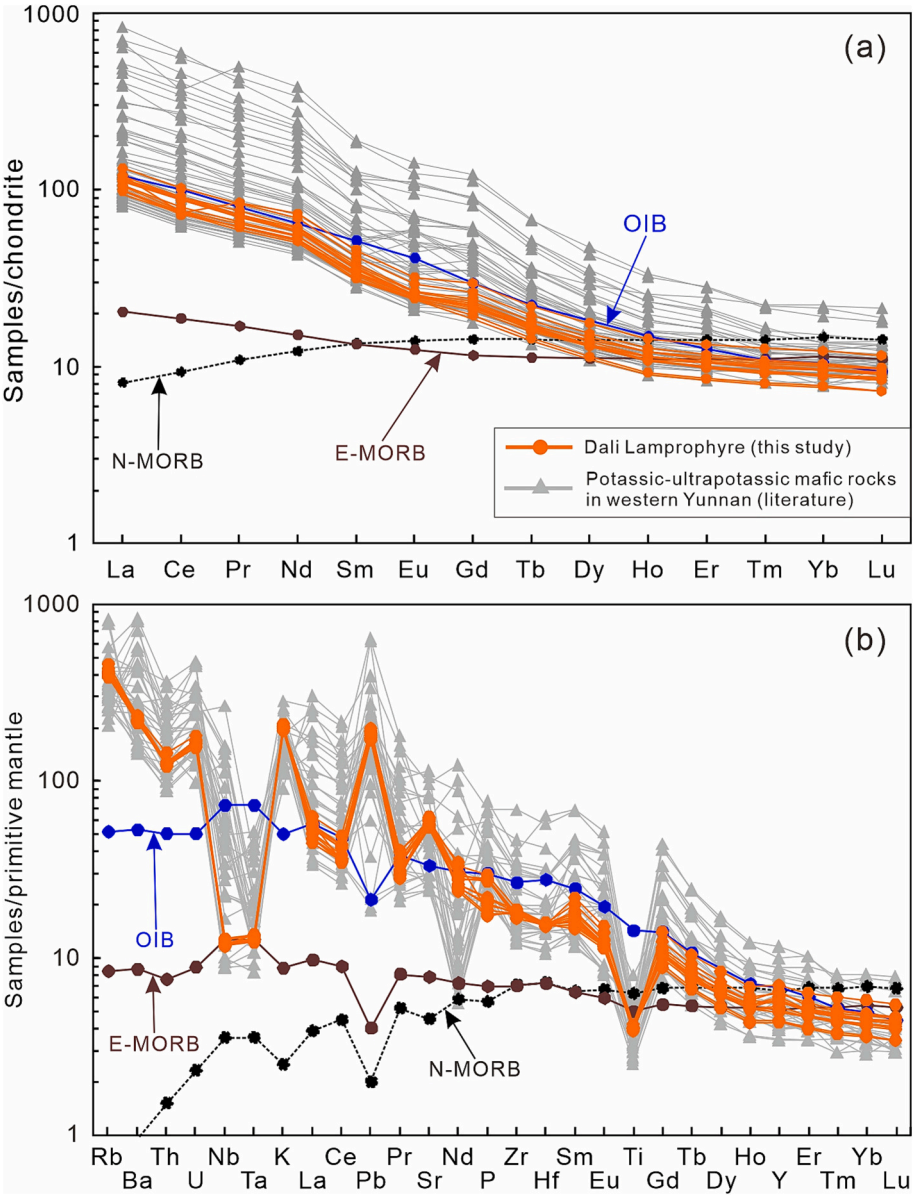

Fig. 5. (a) Chondrite-normalized REE patterns; (b) primitive mantle-normalized multi-element spider diagrams for the Dali lamprophyre. Chondrite and primitive mantle normalizing values are from Boynton (1984) and McDonough and Sun (1995), respectively. Data for the (ultra-)potassic mafic rocks in the southeastern Tibet Plateau are similar to Fig. 4.

Table S4. Overall, Cpx macrocrysts and microcrysts in the lamprophyre and Cpx–Phl nodules have compositions of $En_{34–53}Fs_{1–19}Wo_{42–53}$, with the data fallen mainly into the diopside field, and minor into the augite field (Appendix C. Fig. S2a, b).

Cores of the Cpx macrocrysts have Mg# = 65 to 89 with two clusters (i.e., core I and II) (Fig. 7a): core I has Mg# = 80–89 (peak at 86–88), while core II has lower and less continuous Mg# value (65–80, peak at 76–78) (Fig. 7a). These two types of cores belong to the macrocrysts with normal- and reverse-zoned texture, respectively (Figs. 6a-f and 7a). The oscillatory-zoned mantle has similar Mg# range (62–89, peak at 80–88) (Fig. 7b). The Cpx macrocryst rims have lower Mg# (63–83, peak at 68–80) than their cores and mantles (Fig. 7c). The sieved domains of Cpx macrocrysts have Mg# = 69–87 (two clusters with peaks at 70–74 and 86–88) (Fig. 7d). Moreover, the microcrysts from the lamprophyre host have low Mg# (59–84, peak at 72–78) (Fig. 7e). In contrast, the microcrysts from the Cpx–Phl nodules have high Mg# (78–87), similar to Cpx core I (Fig. 7a, e).

Major and minor element (SiO_2, Al_2O_3, Na_2O, TiO_2 and Cr_2O_3) contents for all the Cpx macrocrysts and microcrysts show large variations (Appendix C. Fig. S3). Overall, the samples have Mg# correlates positively with SiO_2, and negatively with Al_2O_3 and Na_2O (Appendix C. Fig. S3a-f). Correlations between Mg# and TiO_2 and Cr_2O_3 contents are weak (Appendix C. Fig. S3g-j). Microcrysts of Cpx from the Cpx–Phl nodules have similar SiO_2, Al_2O_3, Na_2O and TiO_2 contents to the macrocryst-cores, while their Cr_2O_3 content is relatively higher than the latter (Appendix C. Fig. S3). In contrast, Cpx microcrysts from the lamprophyre host have lower SiO_2 and Cr_2O_3 contents, but higher Al_2O_3, Na_2O and TiO_2 contents than those of microcrysts from the Cpx–Phl nodules (Appendix C. Fig. S3).

Trace element compositions for the different Cpx types are highly variable (Appendix B. Table S5). In the chondrite-normalized REE diagrams, the majority of Cpx macrocrysts and microcrysts show convex upward, with $(La/Yb)_N$ = 0.58 to 7.17 and $(Dy/Yb)_N$ = 1.15 to 3.17 (Fig. 8a, c, e). From the Cpx macrocryst cores to mantle and rims, the ratios of Eu/Eu* varying from 0.71 to 1.16 (avg. 0.92), 0.69 to 1.10 (avg. 0.86) and 0.74 to 0.97 (avg. 0.88), respectively (Appendix B. Table S5;

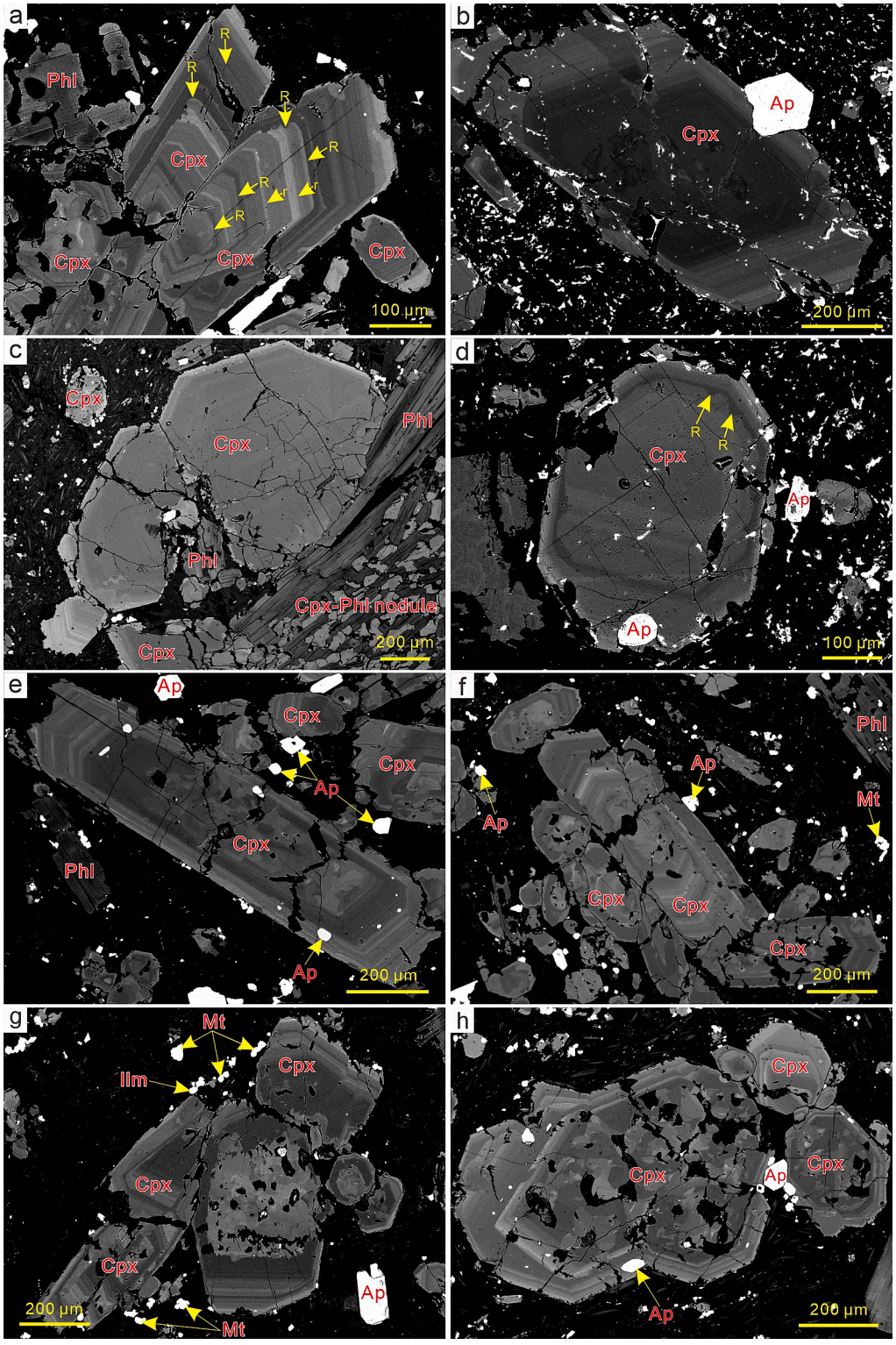

Fig. 6. Back-scattered electron (BSE) images for the different types of Cpx macrocrysts in lamprophyre at Dali: (a) normal oscillatory zoning and coarse layers; (b) normal oscillatory zoning and closely-packed layers; (c) normal oscillatory zoning on the Cpx–Phl nodule margin; (d) normal oscillatory zoning and resorption surface (R); (e) normal oscillatory zoning; (f) reverse oscillatory zoning; (g, h) sieved textures in the core and oscillatory zoned mantle. Abbreviations: Cpx = clinopyroxene; Phl = phlogopite; Ap = apatite; Mt. = magnetite; Ilm = ilmenite.

Fig. 8a, c, e). The high Mg# Cpx macrocryst cores have lower REE contents than their mantle and rims and sieved domain (Fig. 8a, c, e). The high Mg# Cpx microcrysts from Cpx-Phl nodules have similar REE contents with the Cpx macrocryst cores from the hosting lamprophyre. In contrast, the low Mg# Cpx microcrysts from hosting lamprophyre have high REE contents (Fig. 8a, c, e). In the primitive mantle-normalized multi-element spider diagrams, all the Cpx samples show positive Sc but negative Zr, Hf and Ti anomalies (Fig. 8b, d, f). For compatible elements, all the Cpx macrocrysts and microcrysts from the lamprophyre host have commonly low Cr (avg. 225 ppm), but high Co (avg. 32.4 ppm) and Ni (avg. 155 ppm) contents (Appendix B. Table S5). In contrast, Cpx microcrysts from the Cpx–Phl nodules have higher Cr (avg. 1163 ppm) but lower Co (avg. 29.7 ppm) and Ni (avg. 53.4 ppm) contents than the other Cpx macrocryst and microcryst types in the lamprophyre host (Fig. 8b, d, f; Appendix B. Table S5).

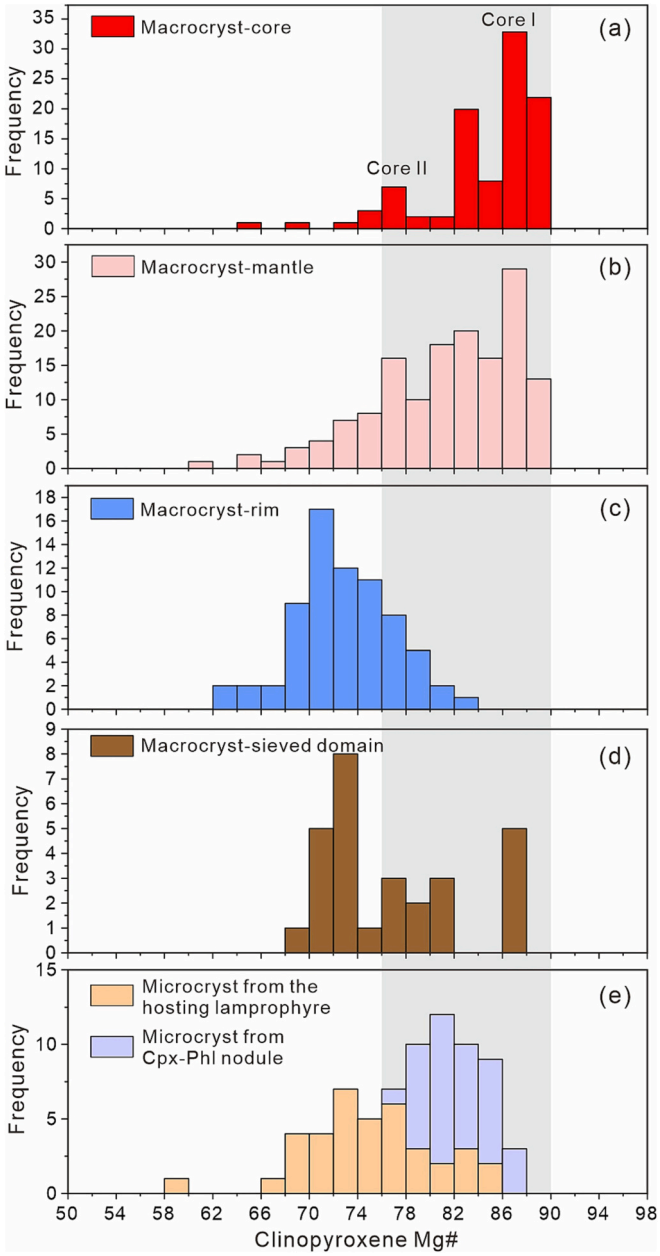

Fig. 7. Mg# histogram for Cpx macrocrysts/microcrysts from the Cpx–Phl nodules and their lamprophyre host.

4.3.3. *Intragrain geochemical profile for Cpx macrocryst*

Cpx macrocrysts with normal- and reverse-zoning and sieved texture show distinct oscillations of Mg, Fe, Al, and Na in the high-resolution elemental X-ray maps (Fig. 9). Cpx macrocrysts with coarse layers and closely-packed layers have commonly Mg-rich cores, oscillatory-zoned mantle, and Fe-Al-Na-rich rims (Fig. 9a, b). Moreover, they clearly show sector zoning of Al and Na in the elemental X-ray maps (Fig. 9a, b). The layers in the prism sectors are relatively Al-rich and slightly Na-rich (Fig. 9a, b). In the BSE image and high-resolution 2-D elemental maps, another Cpx crystal twins with reverse zoning show a resorbed and Fe–Al–Na-rich core, which may represent an inherited core (Fig. 9c). The sieve domain of Cpx macrocryst are enriched in Fe, Al and Na, similar to those of the rim, whereas the oscillatory-zoned mantle displays distinct Mg enrichments (Fig. 9d).

The core-to-rim compositional profiles of Cpx macrocrysts along the long axis also show similar variation major and minor element trends (Fig. 10). Cpx macrocryst with coarse layers typically show high-amplitude oscillation of Mg# and Al_2O_3 on the major resorption surface (Fig. 10a, b). The Mg# on surface with local wavy boundaries varies by ±5 to ±12 relative to neighboring layers (Fig. 10a, b). Moreover, SiO_2 and Cr_2O_3 contents along the profile with coarse layers are also consistent with Mg#, while Al_2O_3, TiO_2 and Na_2O contents shows the opposite trend (Fig. 10a-d). In contrast, the Cpx macrocryst with closely-packed layers display constantly high Mg#, and SiO_2 and Cr_2O_3 contents in the core than the rims, while Al_2O_3, TiO_2 and Na_2O contents show the opposite trend (Fig. 10e-h). The oscillatory-zoned mantle with closely-packed layers and straight boundaries has low-amplitude oscillation of Mg#, Al_2O_3, SiO_2, TiO_2 and Na_2O on the minor resorption surface (Fig. 10e-h). The Mg# of those boundaries varies <3 relative to the neighboring layers (Fig. 10f).

4.3.4. *Clinopyroxene Sr isotope compositions*

In situ Sr isotope compositions of Cpx macrocrysts and microcrysts from the lamprophyre host and the Cpx–Phl nodules are listed in Appendix B. Table S6 and illustrated in Fig. 11. Microcrysts from the lamprophyre host are too fine for the Sr isotope analysis. Overall, the 33 Cpx macrocryst and microcryst spot analyses yielded $^{87}Sr/^{86}Sr = 0.7050$ to 0.7065, mostly below the measured whole-rock ratios slightly ($^{87}Sr/^{86}Sr$ = 0.7061 to 0.7063) (Appendix B. Table S6). In general, $^{87}Sr/^{86}Sr$ ratios have weak negative correlation with Mg# (within a single grain) (Fig. 11a-i). The majority of Cpx samples show weak $^{87}Sr/^{86}Sr$ variations (Fig. 11j). In contrast, the sieved domains of Cpx macrocrysts have wider $^{87}Sr/^{86}Sr$ range (0.7054–0.7065) than that of other Cpx macrocryst and microcryst types (Fig. 11f-i).

5. Discussion

5.1. *Geothermobarometry*

Clinopyroxene–melt thermobarometry is a robust tool for reconstructing pre-eruptive magmatic processes, especially in estimating the Cpx crystallization pressure (Putirka, 2008, 2017). It is necessary to evaluate whether chemical equilibrium existed before any thermobarometric interpretations. The Fe—Mg exchange coefficient based on crystallization temperature (T) is an important test for clinopyroxene-melt equilibrium (Putirka, 2008). However, whole-rock compositions of our Dali lamprophyre sample (with high-Si) cannot represent the equilibrium melts, because they have restricted major element compositions, contrasting with the chemical variability of Cpx that show complex oscillatory zoning and highly variable Mg# (Figs. 4 and 6). We tried to use the coeval (ultra-)potassic rocks (with similar geochemistry to the Dali lamprophyre) in the southeastern Tibet Plateau (e.g., Huang et al., 2010; Lu et al., 2015; Shen et al., 2021; Wang et al., 2021) to match the equilibrium melts of Cpx phenocrysts. Unfortunately, the limited geochemical data are hard to match with the Cpx compositions.

Therefore, we used clinopyroxene-only thermobarometers, i.e., independent from the composition of the melt (Putirka, 2008). Previous studies have shown that Fe—Mg partitioning between Cpx and alkaline mafic rocks can be checked with respect to the ideal range of $K_D(Fe—Mg)^{Cpx\text{-}Liquid} = 0.26 \pm 0.05$ (Akinin et al., 2005; Ubide et al., 2014). In this study, the eq. 32c of Cpx–only barometer and eq. 32d of Cpx–only thermometer was selected to estimate the magma crystallization pressure and temperature, respectively (Putirka, 2008). The $K_D(Fe—Mg)^{Cpx\text{-}Liquid}$ of the Cpx marcocryst cores (with normal zoning and reversed zoning) and Cpx marcocryst rims (incl. Normal and reverse oscillatory zoning and sieved texture) plot within the equilibrium range with values ranging from 0.22 to 0.29 (Appendix B. Table S7; Appendix C. Fig. S4).

Estimated pressure and temperature for the normal zoned Cpx marcocryst high-Mg# cores (Mg# = 77–89) and the Cpx marcocryst low Mg# rims (Mg# = 63–83) are of 580 to1160 MPa (avg. 919 MPa) and 30 to 1270 MPa (avg. 681 MPa), and 1116 to 1266 °C (avg. 1216 °C) and 955 to 1215 °C (avg. 1110 °C), respectively (Fig. 12a, b). These results

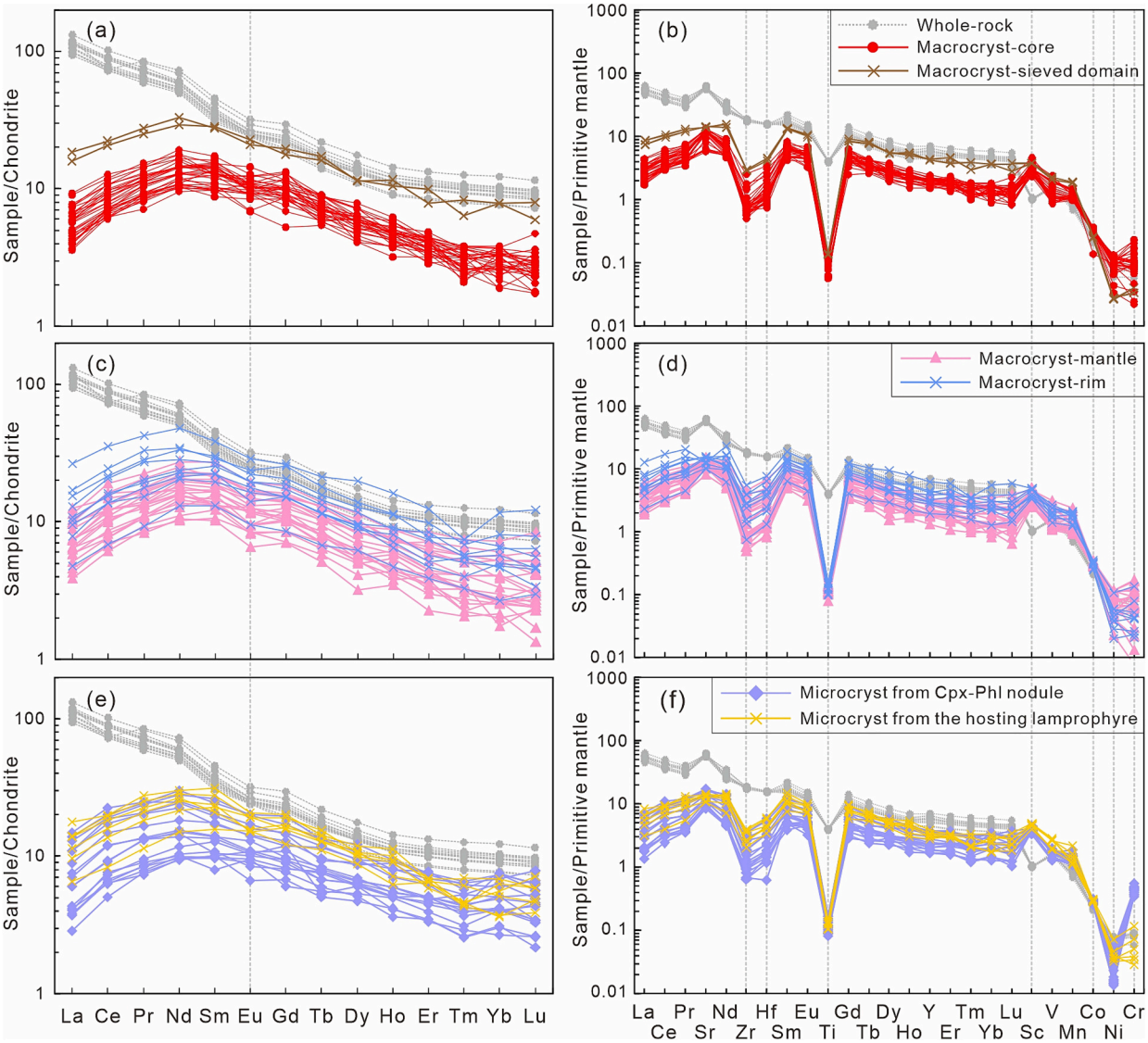

Fig. 8. Chondrite-normalized REE patterns (a, c and e) and primitive mantle-normalized trace element patterns (b, d and f) of Cpx macrocrysts/ microcrysts from the Cpx–Phl nodules and their lamprophyre host. Chondrite and primitive mantle normalizing values are from Boynton (1984) and McDonough and Sun (1995), respectively.

indicate polybaric differentiation or Cpx-saturated magmas. In contrast, the estimated pressure and temperature for the reverse-zoned Cpx marcocryst cores (Mg# = 65–80) vary from 450 to 1310 MPa (avg. 953 MPa) and 1097 to 1209 °C (avg. 1166 °C), respectively (Fig. 12a, b; Appendix B. Table S7). Combined with the petrographic features (Figs. 6f and 9c), these data confirm that the reverse-zoned Cpx marcocrysts cores are likelyformed in equilibrium with a more evolved magma batch, and then were entrapped by more primitive mantle-derived potassic magmas during magma upwelling.

5.2. *Mixing of mantle-sourced magmas*

(Ultra-)potassic mafic rocks in the southeastern Tibet Plateau share similar geochemical features, including the LREE and LILE enrichments, HFSE depletions, and enriched Sr–Nd–Pb isotope compositions (Guo et al., 2005; Huang et al., 2010; Lu et al., 2015; Yu et al., 2020), indicating that they are derived from low-degree partial melting of the metasomatized subcontinental lithospheric mantle (SCLM) (Wang et al., 2021; Xu et al., 2021). The SCLM may be metasomatized by the Neoproterozoic subduction beneath the Yangtze Craton and/or Late Paleozoic Emeishan flood basalt magmatism (Huang et al., 2010; Lu et al., 2015). The coeval Dali lamprophyre dykes have similar geochemical features with the above-mentioned (ultra-)potassic mafic rocks (Fig. 5; Appendix C. Fig. S1), implying probably a similar mantle-derived origin. The complex oscillatory zoning and highly variable Mg# for the Cpx marcocrysts indicate that the Dali lamprophyre dykes may be derived from the same mantle source or from different mantle sources (Humphreys et al., 2006; Ubide et al., 2014; Xing and Wang, 2020). Moreover, the Cpx Mg# vs. La/Yb diagram shows no correlation between them, indicating that the AFC process does not affect the Cpx composition (Appendix C. Fig. 5).

The Cpx-melt REE partition coefficients are usually considered as constant during basaltic magma fractionation or substantial undercooling (Lofgren et al., 2006; Mollo et al., 2013; Winpenny and MacLennan, 2011). Accordingly, the La/Yb and Dy/Yb ratios of melt in equilibrium with Cpx have been widely used to trace the mantle source and partial melting processes for mantle-derived magmatic rocks (Duggen et al., 2005; Prelevic et al., 2012; Xing and Wang, 2020). In this research, the high-Mg# (>85) domains of Cpx macrocrysts/microcrysts were used to evaluate the compositions of equilibrium melts, avoiding possible effects of fractional crystallization and crustal contamination in the crustal magma reservoirs. The calculate formulas and parameters

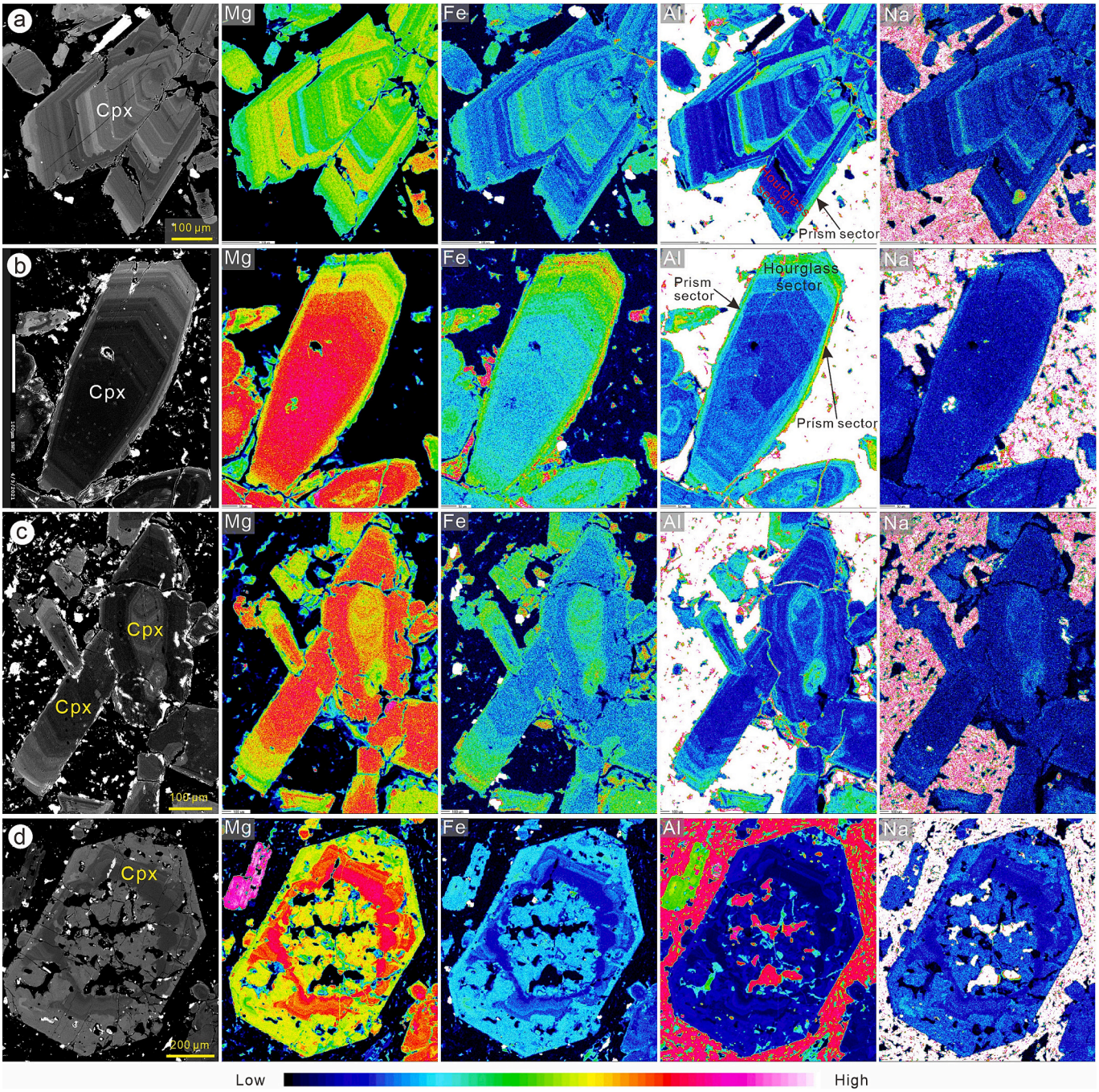

Fig. 9. BSE images and EPMA elemental maps (Mg, Si, Ca, Fe, Al, Na and Cr) for the normal-, reverse zoning and sieved texture of Cpx macrocrysts.

followed those of Prelevic et al. (2012) and Xing and Wang (2020), and the results are illustrated in Fig. 13. The equilibrium melts of Cpx macrocrysts/microcrysts from the Cpx–Phl nodules and their lamprophyre host were calculated, with La/Yb = 16.1–21.5 and 14.3–37.3, and Dy/Yb = 1.66–2.05 and 1.53–2.45 (Fig. 13a, b).

It is widely accepted that a K-rich and water-rich phase (e.g., phlogopite and hornblende) is required in the mantle source to form (ultra-)potassic magmatic rocks (Foley, 1992a, 1992b). A modelling study based on a non-modal, fractional partial melting model was adopted here to evaluate the required garnet- or spinel-field mantle sources. Firstly, modelling for the garnet- and spinel-facies phlogopite harzburgite was carried out (Prelevic et al., 2012), and the partial melting curves show ca. 10–40% partial melting (Fig. 13a, b). However, it is difficult to explain the La/Yb and Dy/Yb variations of the equilibrium melt compositions. Alternatively, the garnet- and spinel-facies phlogopite lherzolite in the model were also adopted as described in Duggen et al. (2005) and Xing and Wang (2020). The results show that magmas of the Dali lamprophyre and their Cpx–Phl nodules were probably derived from similar mantle sources (Fig. 13a, b). La/Yb and Dy/Yb ratios for the magma of the Cpx–Phl nodules and heir lamprophyre host indicate that the magma could be produced by a mixed of 1–2% melting of garnet-phlogopite-bearing lherzolite mantle with 0.5–5% melting of spinel-phlogopite-bearing lherzolite mantle source.

5.3. *Transcrustal magmatic processes*

Mantle-derived magmas would undergo various transcrustal processes before reaching the shallow crust, such as fractional crystallization, assimilation and crustal contamination, and varying degrees of magma mixing/recharge (Handley et al., 2008; Li et al., 2021; Liu et al.,

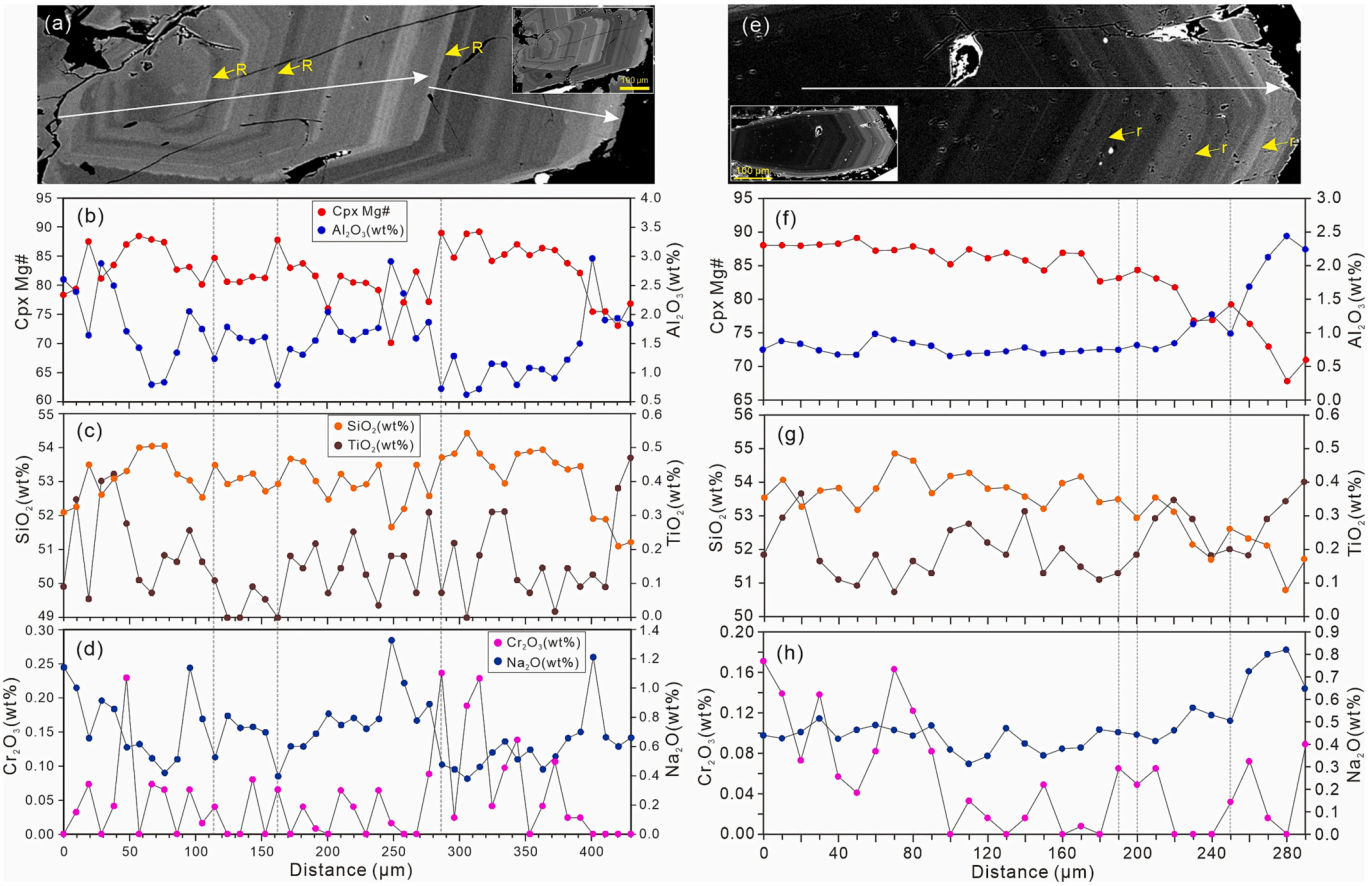

Fig. 10. BSE image (a, e) and major and minor compositional profiles (b-d and f-h) across the Cpx macrocrysts with normal zoning and coarse layers, and closely-packed layers. Major (R) resorption surface is developed; Minor (r) resorption surface is developed.

2014). Previous studies show that the Cenozoic (ultra-)potassic mafic rocks in southeastern Tibet Plateau have undergone extensive fractionation with limited crustal contamination (e.g., Huang et al., 2010; Lu et al., 2015; Yu et al., 2020). The Dali lamprophyre shows distinctly positive correlations between MgO and the Ni, Cr, and CaO contents, indicating extensive clinopyroxene and olivine fractionation (Appendix C. Fig. S6).

The studies of experimental and natural samples show that crystallization conditions and kinetic effects (e.g., degrees of undercooling and/or decompression) may influence the Cpx texture and chemical compositions (Masotta et al., 2020; Mollo et al., 2013; Neave et al., 2019; Xing and Wang, 2020; Zhou et al., 2021). Clinopyroxene marcocrysts in the Dali lamprophyre dyke have well-developed normal and reverse oscillatory zoning and sieved textures suggesting that they may have undergone complex crystal growth process (Fig. 6). Oscillatory zoning is widely reported in plagioclase and clinopyroxene from many volcanic rocks and hypabyssal porphyries, and has been used to trace the crystallization kinetics, magma recharge and convection processes in the crustal-level magma reservoirs (Ginibre et al., 2002a, 2002b, 2007; Humphreys et al., 2006; Li et al., 2021). Oscillatory zoning of our Cpx marcocryst samples display distinct major (R) and minor (r) resorption surface, and variable amplitude oscillations of Mg# and major and minor elements at the layer boundaries (Fig. 10). Experimental studies suggest that resorption surface is attributed to changes of melt composition, heating and/or decompression during crystallization (Ginibre et al., 2002a; Hammouda and Pichavant, 2000; Nelson and Montana, 1992).

A major resorption surface (R) with high-amplitude oscillation of Mg# and major elements probably correlates to a strong magma mixing/recharge event (Davidson and Tepley, 1997; Ginibre et al., 2002a), while a minor resorption surface (r) with low-amplitude oscillation of Mg# and major elements may indicate a local magma mixing or local kinetic effect on the growth of Cpx marcocryst due to dynamic convection (Elardo and Shearer, 2014; Ginibre et al., 2002a, 2002b; Xing and Wang, 2020). The typical profiles of Cpx marcocryst with coarse layers show distinct high-amplitude Mg# oscillation at the major resorption surface (Fig. 10a-d), similar to those of Cpx marcocrysts from an ultrapotassic lamprophyre dyke in the Ortok Mountain, Kyrgyzstan (Xing and Wang, 2020). In these profiles, Cr concentration is positively correlated with Mg#, due to its compatible behavior in the Cpx lattice (Fig. 10b, d). Moreover, a crystal twin of Cpx marcocryst with coarse layers shows that the major resorption surface crosscut several oscillatory zones (Fig. 6a), indicating that a more primitive magma recharge may have caused temperature increase and dissolution, followed by compositional change and reprecipitation (Ginibre et al., 2002a; Xing and Wang, 2020). In contrast, the closely-packed layers with straight boundaries in the Cpx marcocryst display high-frequency and low-amplitude Mg# oscillations (Fig. 10e-h), suggesting local magma mixing with similar magma compositions or local kinetic effect in the boundary layers at the crystal-melt interface (Ginibre et al., 2002a).

The sieve texture occurs in the Cpx marcocryst cores, with many phlogopite and matrix filling into the spongy space and linking the external groundmass by irregular or saw-toothed cracks (Figs. 6g, h and 9d). This textural feature is commonly attributed to melt composition changes, cooling and/or decompression during crystallization (Humphreys et al., 2006; Neave and MacLennan, 2020; Pan et al., 2018; Xing and Wang, 2020). In general, Cpx crystallization under substantial undercooling could produce skeletal or dendritic texture, such as sector zoning (Ubide et al., 2019; Welsch et al., 2016; Zhou et al., 2021). During this rapid skeletal growth, the pores in Cpx may be filled by the

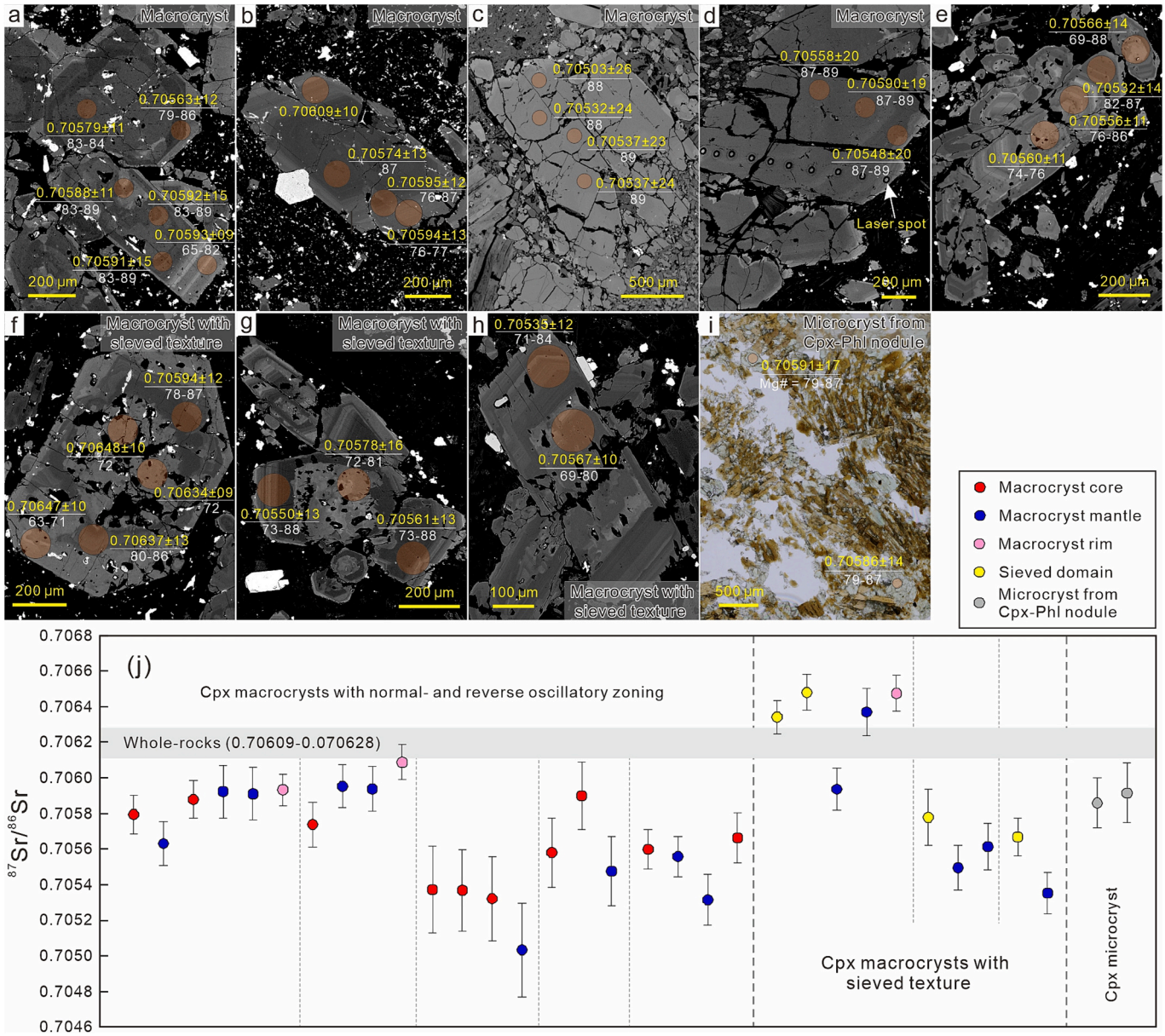

Fig. 11. In situ Sr isotope compositions of the various Cpx macrocrysts/microcrysts from the Cpx–Phl nodules and their lamprophyre host.

matrix and/or mica (Masotta et al., 2020; Zhou et al., 2021). However, sector zoning is not found in the sieved domain of Cpx marcocryst samples in this study. Rapid decompression may produce coarse sieve texture on the rim of Cpx marcocrysts in mantle xenoliths (Pan et al., 2018). This spongy rim has commonly higher Mg#, Ca and Cr contents, but lower Al and Na contents than those of the primary Cpx (Pan et al., 2018). Moreover, rapid decompression in volcanic rock formation could lead to distinct low Al_2O_3 content in the Cpx marcocryst rim (Neave and MacLennan, 2020). On the contrary, the sieve domain in the Cpx marcocryst core has similar major and minor compositions and $^{87}Sr/^{86}Sr$ ratios with those of the rim (Figs. 9d and 11f-h), excluding the effect of rapid decompression during crystal growth. We note that the sieved domain has heterogeneous composition and uneven margins connecting with their oscillatory-zoned mantle (Figs. 6g, h and 11f-h), suggesting an origin by Cpx dissolution as the effect of groundmass melt propagating through cracks, which are similar to the case of the Ortok ultrapotassic lamprophyre dykes, Kyrgyzstan (Xing and Wang, 2020). Therefore, the sieved texture of our Cpx marcocryst samples may have been formed by dissolution and reprecipitation during magma solidification.

As the above La/Yb and Dy/Yb modelling result, the Cpx–Phl nodules and lamprophyre host may probably derived from similar mantle sources. Petrographic features shown that the nodules and their lamprophyre host have similar mineral assemblages (Fig. 2b-e). Moreover, Cpx microcrysts from the Cpx–Phl nodules have distinctly higher Cr but lower Co and Ni contents than the other Cpx macrocrysts/microcrysts in the Dali lamprophyre host, suggesting they probably formed by accumulation of minerals fractionated from a minette more primitive than the host. Similar case studies for Cpx–Phl nodules are also reported from the diverse potassic lamprophyre and other lavas worldwide (Righter and Rosas-elguera, 2001; Semiz et al., 2012; Soltanmohammadi et al., 2021).

6. Conclusions

1. Three types of Cpx macrocrysts, i.e., those with normal- and reverse oscillatory zoning and sieved textures, and Cpx microcrysts from Cpx–Phl nodules, are identified in the Cenozoic Dali lamprophyre dyke.

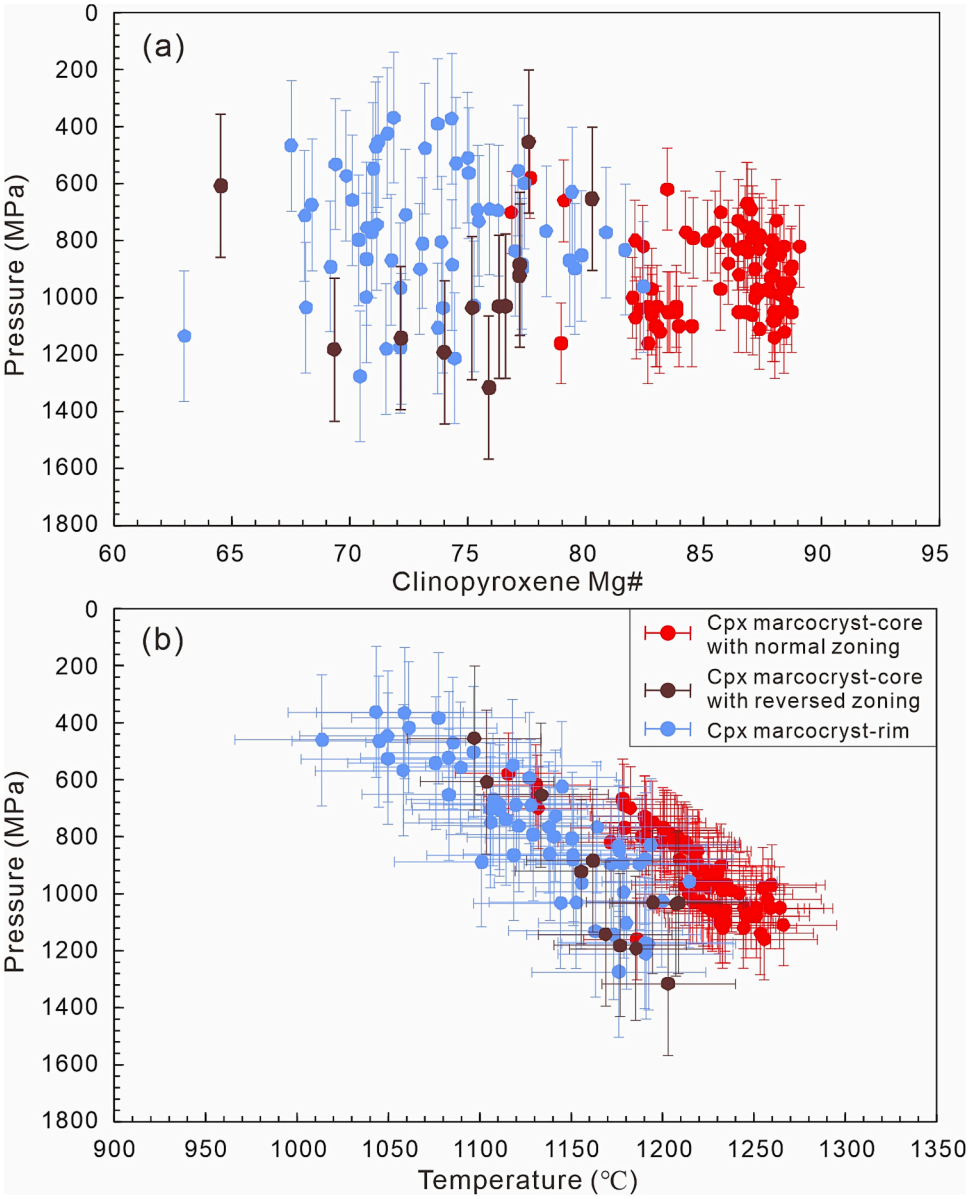

Fig. 12. Crystallization pressure and temperature for the matched core and rim of Cpx macrocrysts. Temperature and pressure were calculated using the Cpx–only thermometer and the Cpx–only barometer (Putirka et al., 2008).

2. The La/Yb and Dy/Yb modelling of equilibrium melts suggests that magmas of the Cpx–Phl nodules and their lamprophyre host were probably derived from similar mantle sources.
3. Oscillatory zoning of Cpx macrocrysts with coarse layers and major resorption surface record multiple magma mixing/recharging events, while Cpx macrocrysts with closely-packed layers and minor resorption surface suggest local magma mixing or crystal-melt interface reaction. The sieved domain of Cpx marcocryst was formed by dissolution and reprecipitation during magma solidification.
4. The Cpx–Phl nodules were probably formed by accumulation of minerals fractionated from a minette more primitive than the lamprophyre host.

Supplementary data to this article can be found online at https://doi.org/10.1016/j.lithos.2023.107281.

Declaration of Competing Interest

We have no known competing financial interests or personal relationships that could have appeared to influence the work reported in this paper.

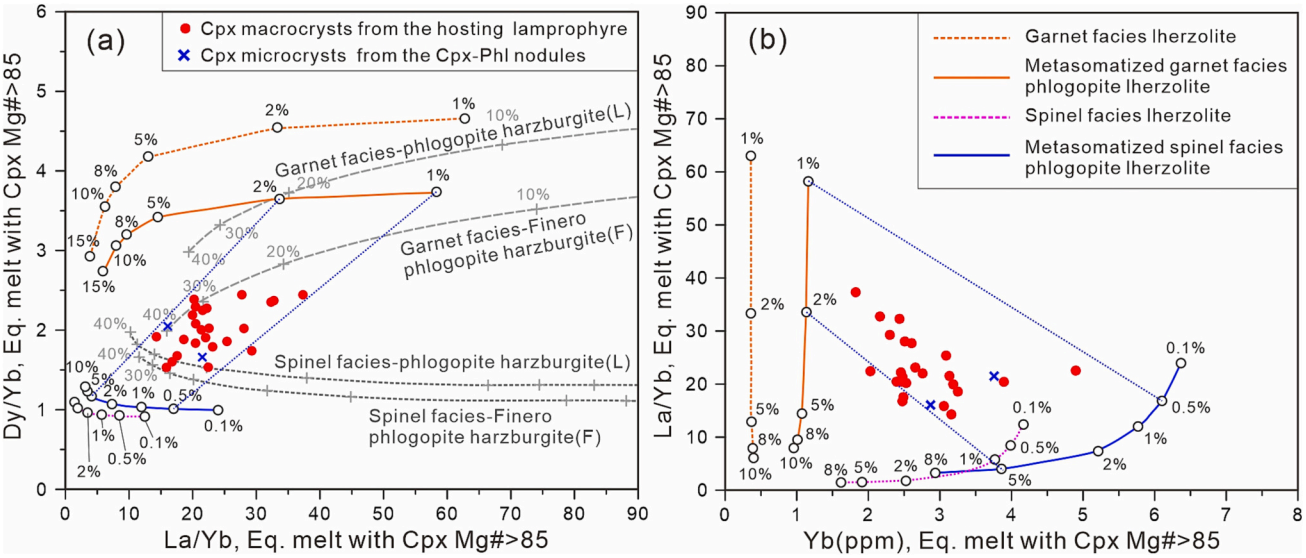

Fig. 13. Binary plots of calculated La/Yb vs. Dy/Yb (a) and Yb vs. Dy/Yb (b) of melts in equilibrium with Cpx macrocrysts/microcrysts (Mg# >85) from the Cpx–Phl nodule and their lamprophyre host. Partition coefficients of $D_{Cpx\text{-}melt}$ La, Dy, Yb are 0.029, 0.33 and 0.22, respectively (Prelevic et al., 2012). Melting curves of the metasomatized garnet−/spinel-facies phlogopite harzburgite (L), and the metasomatized garnet−/spinel-facies finero phlogopite harzburgite (F) are from Prelevic et al. (2012). The other geochemical parameters are similar to Xing and Wang (2020). The equation C_{Melt} i = C_{Cpx} i/$D_{Cpx/Melt}$ i, where C_{Melt} i and C_{Cpx} i = concentration of element i in melt and clinopyroxene, respectively, and $D_{Cpx/Melt}$ i = partition coefficient of i between clinopyroxene and melt.

Acknowledgements

This study was financially supported by the National Key Research and Development Project (2019YFA0708601). We would like to thank Dr. Ningchao Zhou (Xi'an Center of Geological Survey) and Dr. Gaobin Chu (Guangzhou Institute of Geochemistry, Chinese Academy of Sciences) for assisting with the EPMA and in situ Sr isotope analysis, respectively. Thanks also to Drs. Zhongjie Bai (Institute of Geochemistry, Chinese Academy of Sciences, Guiyang, China), and Renzhi Zhu and Xiaojun Wang (Northwest University, Xi'an, China) for the fruitful discussion, and to Dr. Bei Chen (Australian National University, Canberra, Australia) and Xinchao Yuan (Northwest University, Xi'an, China) for helping with the field work and sample collection.

References

Akinin, V.V., Sobolev, A.V., Ntaflos, T., Richter, W., 2005. Clinopyroxene megacrysts from Enmelen melanephelinitic volcanoes (Chukchi Peninsula, Russia): application to composition and evolution of mantle melts. Contrib. Mineral. Petrol. 150, 85–101.

Boynton, W.V., 1984. Cosmochemistry of the Rare Earth Elements: Meteorite Studies// Henderson P. Rare Earth Element Geochemistry Developments in Geochemistry. Elsevier, Amsterdam, pp. 115–1522.

Casetta, F., Ickert, R.B., Mark, D.F., Bonadiman, C., Giacomoni, P.P., Ntaflos, T., Coltorti, M., 2019. The Alkaline Lamprophyres of the Dolomitic Area (Southern Alps, Italy): Markers of the late Triassic Change from Orogenic-like to Anorogenic Magmatism. J. Petrol. 60 (6), 1263–1298.

Cashman, K.V., Sparks, R.S.J., Blundy, J.D., 2017. Vertically extensive and unstable magmatic systems: a unified view of igneous processes. Science 355 eaag3055.

Chung, S.L., Chu, M.F., Zhang, Y.Q., Xie, Y.W., Lo, C.H., Lee, T.Y., Lan, C.Y., Li, X.H., Zhang, Q., Wang, Y.Z., 2005. Tibetan tectonic evolution inferred from spatial and temporal variations in post-collisional magmatism. Earth Sci. Rev. 68, 173–196.

Davidson, J.P., Tepley, F.J., 1997. Recharge in volcanic system: evidence from isotope profiles of phenocrysts. Science 275, 826–829.

Duggen, S., Hoernle, K., van den Bogaard, P., Garbe-Schönberg, D., 2005. Post-collisional transition from subduction- to intraplate-type magmatism in the westernmost Mediterranean: evidence for continental-edge delamination of subcontinental lithosphere. J. Petrol. 46, 1155–1201.

Elardo, S., Shearer, C.J.R., 2014. Magma chamber dynamics recorded by oscillatory zoning in pyroxene and olivine phenocrysts in basaltic lunar meteorite Northwest Africa 032. Am. Mineral. 99, 355–368.

Foley, S.F., 1992a. Petrological characterization of the source components of potassic magmas: geochemical and experimental constraints. Lithos 28, 187–204.

Foley, S.F., 1992b. Vein-plus-wall-rock melting mechanisms in the lithosphere and the origin of potassic alkaline magmas. Lithos 28, 435–453.

Foley, S.F., Venturelli, G., Green, D.H., Toscani, L., 1987. The ultrapotassic rocks: characteristics, classification, and constraints for petrogenetic models. Earth Sci. Rev. 24, 81–134.

Ginibre, C., Kronz, A., Wörner, G., 2002a. High-resolution quantitative imaging of plagioclase composition using accumulated backscattered electron images: new constraints on oscillatory zoning. Contrib. Mineral. Petrol. 142, 436–448.

Ginibre, C., WoRner, G., Kronz, A., 2002b. Minor- and trace-element zoning in plagioclase: implications for magma chamber processes at Parinacota volcano, northern Chile. Contrib. Mineral. Petrol. 143, 300–315.

Ginibre, C., Worner, G., Kronz, A., 2007. Crystal zoning as an archive for magma evolution. Elements 3, 261–266.

Guo, Z.F., Hertogen, J., Liu, J., Pasteels, P., Boven, A., Punzalan, L., He, H., Luo, X., Zhang, W., 2005. Potassic magmatism in Western Sichuan and Yunnan provinces, SE Tibet, China: petrological and geochemical constraints on petrogenesis. J. Petrol. 46, 33–78.

Hammouda, T., Pichavant, M., 2000. Melting of fluorophlogopite plagioclase pairs at 1 atmosphere. Eur. J. Mineral. 12, 315–328.

Handley, H.K., Turner, S.P., Smith, I.E., Stewart, R.B., Cronin, S.J., 2008. Rapid timescales of differentiation and evidence for crustal contamination at intra-oceanic arcs: geochemical and U–Th–Ra–Sr–Nd isotopic constraints from Lopevi Volcano, Vanuatu, SW Pacific. Earth Planet. Sci. Lett. 273, 184–194.

Hart, S.R., 1984. A large-scale isotope anomaly in the southern hemisphere mantle. Nature 309, 753–757.

Huang, X.L., Niu, Y., Xu, Y.G., Chen, L.L., Yang, Q.J., 2010. Mineralogical and Geochemical constraints on the petrogenesis of post-collisional potassic and ultrapotassic rocks from Western Yunnan. J. Petrol. 51, 1617–1654.

Humphreys, M.C.S., Blundy, J.D., Sparks, R.S.J., 2006. Magma evolution and open-system processes at Shiveluch volcano: insights from phenocryst zoning. J. Petrol. 47, 2303–2334.

Imaoka, T., Kawabata, H., Nagashima, M., Nakashima, K., Kamei, A., Yagi, K., Itaya, T., Kiji, M., 2017. Petrogenesis of an early cretaceous lamprophyre dike from Kyoto Prefecture, Japan: implications for the generation of high-Nb basalt magmas in subduction zones. Lithos 291, 18–33.

Karsli, O., Dokuz, A., Kaliwoda, M., Uysal, I., Aydin, F., Kandemir, R., Fehr, K.T., 2014. Geochemical fingerprints of late Triassic calc-alkaline lamprophyres from the eastern Pontides, NE Turkey: a key to understanding lamprophyre formation in a subduction-related environment. Lithos 197, 181–197.

Le Maitre, R.W., Streckeisen, A., Zanettin, B., Le Bas, M.J., Bonin, B., Bateman, P., Bellieni, G., Dudek, A., Efremova, S., Keller, J., Lameyre, J., Sabine, P.A., Schmid, R., Sørensen, H., Woolley, A.R., 2002. Igneous Rocks. A Classification and Glossary of terms. Recommendations of the IUGS Subcomission on the Systematics of Igneous Rocks. Cambridge University Press, Cambridge, pp. 1–236.

Li, W., Yang, Z., Chiaradia, M., Zhou, L., Hou, Z., 2021. Enrichment Nature of Ultrapotassic Rocks in Southern Tibet Inherited from their Mantle Source. J. Petrol. 62 (8), 1–15.

Liu, D., Zhao, Z., Zhu, D.C., Niu, Y., Harrison, T.M., 2013. Zircon xenocrysts in Tibetan ultrapotassic magmas: imaging the deep crust through time. Geology 42, 43–46.

Liu, D., Zhao, Z., Zhu, D., Niu, Y., DePaolo, D.J., Harrison, T.M., Mo, X., Dong, G., Zhou, S., Sun, C., Zhang, Z., Liu, J., 2014. Postcollisional potassic and ultrapotassic rocks in southern Tibet: mantle and crustal origins in response to India–Asia collision and convergence. Geochim. Cosmochim. Acta 143, 207–231.

Lofgren, G.E., Huss, G.R., Wasserburg, G.J., 2006. An experimental study of trace-element partitioning between Ti–Al-clinopyroxene and melt: equilibrium and kinetic effects including sector zoning. Am. Mineral. 91, 1596–1606.
Lu, Y.J., McCuaig, T.C., Li, Z.X., Jourdan, F., Hart, C.J.R., 2015. Paleogene post-collisional lamprophyres in western Yunnan, western Yangtze Craton: Mantle source and tectonic implications. Lithos 233, 139–161.
Ma, L., Jiang, S.Y., Hofmann, A.W., Dai, B.Z., Hou, M.L., Zhao, K.D., Chen, L.H., Li, J.W., Jiang, Y.H., 2014. Lithospheric and asthenospheric sources of lamprophyres in the Jiaodong Peninsula: a consequence of rapid lithospheric thinning beneath the North China Craton? Geochim. Cosmochim. Acta 124, 250–271.
Masotta, M., Pontesilli, A., Mollo, S., Armienti, P., Ubide, T., Nazzari, M., Scarlato, P., 2020. The role of undercooling during clinopyroxene growth in trachybasaltic magmas: Insights on magma decompression and cooling at Mt. Etna volcano. Geochim. Cosmochim. Acta 268, 258–276.
McDonough, W.F., Sun, S.S., 1995. The composition of the Earth. Chem. Geol. 120, 223–253.
Middlemost, E.A., 1994. Naming materials in the magma/igneous rock system. Earth Sci. Rev. 37, 215–224.
Miller, C.F., Wark, D.A., 2007. Supervolcanoes and their explosive supereruptions. Elements 4, 11–16.
Mollo, S., Putirka, K., Misiti, V., Soligo, M., Scarlato, P., 2013. A new test for equilibrium based on clinopyroxene–melt pairs: clues on the solidification temperatures of Etnean alkaline melts at post-eruptive conditions. Chem. Geol. 352, 92–100.
Muravyeva, N.S., Belyatsky, B.V., Senin, V.G., Ivanov, A.V., 2014. Sr–Nd–Pb isotope systematics and clinopyroxene–host disequilibrium in ultra-potassic magmas from Toro-Ankole and Virunga, East-African Rift: implications for magma mixing and source heterogeneity. Lithos 210–211, 260–277.
Neave, D.A., MacLennan, J., 2020. Clinopyroxene dissolution records rapid magma ascent. Front. Earth Sci. 8, 188.
Neave, D.A., Bali, E., Guðfinnsson, G.H., Halldo'rsson, S.A., Kahl, M., Schmidt, A.S., Holtz, F., 2019. Clinopyroxene–liquid equilibria and geothermobarometry in natural and experimental tholeiites: the 2014–2015 Holuhraun eruption, Iceland. J. Petrol. 60, 1653–1680.
Nelson, S.T., Montana, A., 1992. Sieve-textured plagioclase in volcanic rocks produced by rapid decompression. Am. Mineral. 77, 1242–1249.
Pan, S., Zheng, J.P., Yin, Z., Griffin, W., Xia, M., Lin, A., Zhang, H., 2018. Spongy texture in mantle clinopyroxene records decompression-induced melting. Lithos 320–321, 144–154.
Prelevic, D., Foley, S.F., Romer, R.L., Cvetkovic, V., Downes, H., 2005. Tertiary ultrapotassic volcanism in Serbia: constraints on petrogenesis and mantle source characteristics. J. Petrol. 46, 1443–1487.
Prelevic, D., Akal, C., Foley, S.F., Romer, R.L., Stracke, A., Van Den Bogaard, P., 2012. Ultrapotassic mafic rocks as geochemical proxies for post-collisional dynamics of orogenic lithospheric mantle: the case of Southwestern Anatolia. J. Petrol. 53, 1019–1055.
Putirka, K.D., 2008. Thermometers and barometers for volcanic systems. Rev. Mineral. Geochem. 69, 61–120.
Putirka, K., 2017. Down the crater: where magmas are stored and why they erupt. Elements 13, 11–16.
Righter, K., Rosas-elguera, J., 2001. Alkaline lavas in the volcanic front of the western Mexican volcanic belt: geology and petrology of the Ayutla and Tapalpa volcanic fiels. J. Petrol. 42 (12), 2333–2361.
Rock, N.M.S., 1977. The nature and origin of lamprophyres: some definitions, distinctions, and derivations. Earth Sci. Rev. 13, 123–169.
Rock, N.M.S., 1991. Lamprophyres. Blackie, Glasgow, p. 285.
Semiz, B., Hakan Çoban, H., Roden, M.F., Özpınar, Y., Flower, M.F.J., McGregor, H., 2012. Mineral composition in cognate inclusions in late Miocene–early Pliocene potassic lamprophyres with affinities to lamproites from the Denizli region, Western Anatolia, Turkey: Implications for uppermost mantle processes in a back-arc setting. Lithos 134–135, 253–272.
Shen, Y., Zheng, Y.C., Hou, Z.Q., Zhang, A.P., Huizenga, J.M., Wang, Z.X., Wang, L., 2021. Petrology of the Machangqing complex in Southeastern Tibet: Implications for the Genesis of Potassium-rich Adakite-like Intrusions in Collisional zones. J. Petrol. 62 (11), 1–40.
Soltanmohammadi, A., Grégoire, M., Ceuleneer, G., Benoit, M., Bédard, L.P., Gouy, S., Rabinowicz, M., 2021. Origin of Antecrysts in Igneous Rocks from the Salavat Range (NW Iran): an Explanation for the Geochemical Signature of Potassic Alkaline Rocks. J. Petrol. 1–27.
Tappe, S., Foley, S.F., Jenner, G.A., Heaman, L.M., Kjarsgaard, B.A., Romer, R.L., 2006. Genesis of Ultramafic Lamprophyres and Carbonatites at Aillik Bay, Labrador: a consequence of Incipient Lithospheric Thinning beneath the North Atlantic Craton. J. Petrol. 47 (7), 1261–1315.
Ubide, T., Kamber, B.S., 2018. Volcanic crystals as time capsules of eruption history. Nat. Commun. 9, 326.
Ubide, T., Gale, C., Arranz, E., Lago, M., Larrea, P., 2014. Clinopyroxene and amphibole crystal populations in a lamprophyre sill from the Catalonian Coastal Ranges (NE Spain): a record of magma history and a window to mineral–melt partitioning. Lithos 184–187, 225–242.
Ubide, T., Mollo, S., Zhao, J.X., Nazzari, M., Scarlato, P., 2019. Sector-zoned clinopyroxene as a recorder of magma history, eruption triggers, and ascent rates. Geochim. Cosmochim. Acta 251, 265–283.
Wang, R., Luo, C.H., Xia, W.J., He, W.Y., Liu, B., Huang, M.L., Hou, Z.Q., Zhu, D.C., 2021. Role of Alkaline Magmatism in Formation of Porphyry Deposits in Nonarc Settings: Gangdese and Sanjiang Metallogenic Belts. SEG Spec. Publicat. 24 (2), 205–229.
Welsch, B., Hammer, J., Baronnet, A., Jacob, S., Hellebrand, E., Sinton, J., 2016. Clinopyroxene in postshield Haleakala ankaramite: 2. Texture, compositional zoning and supersaturation in the magma. Contrib. Mineral. Petrol. 171, 6.
Winpenny, B., MacLennan, J., 2011. A partial record of mixing of mantle melts preserved in Icelandic phenocrysts. J. Petrol. 52, 1791–1812.
Xing, C.M., Wang, C.Y., 2020. Periodic Mixing of Magmas Recorded by Oscillatory Zoning of the Clinopyroxene Macrocrysts from an Ultrapotassic Lamprophyre Dyke. J. Petrol. 1–26 https://doi.org/10.1093/petrology/egaa103.
Xu, B., Hou, Z.Q., Griffin, W.L., Zheng, Y.C., Wang, T., Guo, Z., 2021. Cenozoic lithospheric architecture and metallogenesis in Southeastern Tibet. Earth Sci. Rev. 214, 103472.
Yang, Z.Y., Jiang, S.Y., 2018. Diverse lamprophyres origins corresponding to lithospheric thinning: a case study in the Jiurui district of Middle-lower Yangtze River Belt, South China Craton. Gondwana Res. 54, 62–80.
Yu, H., Deng, J., Wang, Q., Yang, L., Li, H., Wang, X., 2020. Petrogenesis of Paleogene lamprophyres in the Ailaoshan tectonic belt, western Yangtze Craton: Implications for the mantle source of orogenic gold deposits. Ore Geol. Rev. 122, 103507.
Zellmer, G.F., 2021. Gaining acuity on crystal terminology in volcanic rocks. B Volcanol 83, 78. https://doi.org/10.1007/s00445-021-01505-9.
Zhang, S., Ma, Q., Chen, H., Long, X., Chu, G., Cheng, J., Xia, X., Li, R., 2021. Precambrian crust growth and reworking of the eastern Yangtze Craton: insights from xenocrystic zircons in the lamprophyres from the Middle–lower Yangtze Belt, China. Precambrian Res. 355, 106121.
Zhou, J.S., Wang, Q., Xing, C.M., Ma, L., Hao, L.L., Li, Q.W., Wang, Z.L., Huang, T.Y., 2021. Crystal growth of clinopyroxene in mafic alkaline magmas. Earth Planet. Sci. Lett. 568, 117005.
Zindler, A., Hart, S.R., 1986. Chemical geodynamics. Annu. Rev. Earth Planet Sci. 14, 493–571.